Global oceanic microseism sources as seen by seismic arrays and predicted by wave action models.

Gregor Hillers, Nicholas Graham, Michel Campillo, S. Kedar, Matthieu Landès, N.M. Shapiro

Geochemistry Geophysics Geosystems G3

Article
Volume 13, Number 1
31 January 2012
Q01021, doi:10.1029/2011GC003875
ISSN: 1525-2027

Published by AGU and the Geochemical Society

Global oceanic microseism sources as seen by seismic arrays and predicted by wave action models

G. Hillers
Institut des Sciences de la Terre, Université Joseph Fourier, CNRS, BP 53, F-38041 Grenoble CEDEX 9, France (hillersg@ujf-grenoble.fr)

N. Graham
Hydrologic Research Center, 12780 High Bluff Drive, Suite 250, San Diego, California 92130, USA

M. Campillo
Institut des Sciences de la Terre, Université Joseph Fourier, CNRS, BP 53, F-38041 Grenoble CEDEX 9, France

S. Kedar
Jet Propulsion Laboratory, California Institute of Technology, 4800 Oak Grove Drive, MS 238-600, Pasadena, California 91109, USA

M. Landès
Commissariat à l'Energie Atomique et aux énergies renouvelables, Direction des applications militaires, Department Île-de-France, Bruyeres le Chatel, F-91297 Arpajon, France

N. Shapiro
Institut de Physique du Globe de Paris, Sorbonne Paris Cité, CNRS (UMR7154), F-75238 Paris, France

[1] We analyze global microseism excitation patterns between July 2000 and June 2001. Seismological observations are compared with modeling results to isolate robust activity features of relevant source processes. First, we use observations of microseism source locations estimated by Landès et al. (2010) based on array processing of ambient noise correlations. Second, we construct synthetic activity patterns by coupling sea state estimates derived from wave action models to the excitation theory for microseisms. The overall spatiotemporal evolution of both estimates is characterized by a seasonal character that is associated with strong activity during winter months. The distribution of landmass causes seasonal changes on the Northern Hemisphere (NH) to exceed the variability on the Southern Hemisphere (SH). Our systematic comparison of the two estimates reveals significant microseism excitation along coastlines and in the open ocean. Since coastal reflections are not accounted for in the modeling approach, the consistent mismatch between near-coastal observations and predictions suggests that relevant microseism energy arriving at the networks is generated in these areas. Simultaneously, systematic coincidence away from coastlines verifies the open ocean generation hypothesis. These conclusions are universal and robust with respect to the seismic network locations on the NH. The spatially homogeneous resolution of our synthetics provides a valuable resource for the assessment of the global microseism weather. Similar to previously identified hot spot areas in the North Atlantic, the modeled distributions hypothesize regions of strong localized activity on the SH, which are only partially confirmed by the analyzed data sets.

Components: 10,700 words, 10 figures.

Keywords: microseisms; noise seasonality; noise source; seismic noise; wave action models.

Index Terms: 4504 Oceanography: Physical: Air/sea interactions (0312, 3339); 7203 Seismology: Body waves.

Received 15 September 2011; **Revised** 19 December 2011; **Accepted** 19 December 2011; **Published** 31 January 2012.

Hillers, G., N. Graham, M. Campillo, S. Kedar, M. Landès, and N. Shapiro (2012), Global oceanic microseism sources as seen by seismic arrays and predicted by wave action models, *Geochem. Geophys. Geosyst.*, *13*, Q01021, doi:10.1029/2011GC003875.

1. Introduction

[2] Microseisms constitute the most energetic seismic background noise observed around the globe [*McNamara and Buland*, 2004; *Berger et al.*, 2004]. They are known to result from nonlinear interactions between the atmosphere, the oceans, and solid Earth [*Longuet-Higgins*, 1950; *Hasselmann*, 1963], with atmospheric forcing, predominantly surface winds, being the main source. The availability of decades of seismic records makes microseisms a target resource for the study of the variability of climatic processes [*Bromirski and Duennebier*, 2002; *Aster et al.*, 2010]. Microseisms have also been receiving increasing appreciation by Earth scientists for the extraction of deterministic information from the associated random seismic wavefield [*Shapiro and Campillo*, 2004; *Courtland*, 2008], which was previously only regarded as a nuisance that hampered the analysis of impulsive phases associated with earthquakes and explosions.

[3] The less energetic, single-frequency microseisms peak at periods around 14 s is a consequence of direct interactions between coastal seas and shallow bathymetry. The stronger double-frequency peak at 7 s results from nonlinear wave-wave interactions between ocean gravity waves [*Longuet-Higgins*, 1950]. Pressure fluctuations induced by waves with the same period propagating in opposite directions are modulated by the height of the resonating water column. The transmitted microseism energy therefore depends on ocean wave state and bathymetry.

[4] Opposing wave patterns arise through two primary mechanisms. First, they can occur when a (generally very small) fraction of the incoming wave incident on a coastline is reflected back, seaward [*Elgar et al.*, 1994]. Under favorable circumstances, the portions of the incoming and reflected wave energy propagate in opposite directions. The resulting microseism episodes seen in seismic records have long been identified with large waves arriving at coastlines [*Wiechert*, 1904; *Gutenberg*, 1924]. The strength of the reflection and of the resulting magnitude of excitation is sensitive to many factors. These include the approach angle of the incoming waves, the coastline orientation, inshore bathymetry, the beach slope, and the breaker zone characteristics. Hence, the magnitude and directional dispersion of wave energy reflected from coastlines are difficult to quantify through observations or modeling.

[5] The second primary mechanism for opposing wave patterns is association with midlatitude storm systems [*Kedar et al.*, 2008; *Kedar*, 2011] and tropical cyclones [e.g., *Zhang et al.*, 2010] in the open oceans. In this mechanism, waves of the same period generated in different parts of the wind field surrounding a low-pressure system, or in separate lows, cross at opposing angles. *Kedar et al.* [2008] demonstrated the correlation between observed microseism energy and such sea states over amplifying bathymetry in the North Atlantic Ocean during Northern Hemisphere (NH) winter. This proved earlier observations of pelagic excitation [e.g., *Cessaro*, 1994]. The demonstrated possibility to resolve and monitor double-frequency noise excitation in coastal and pelagic areas is of interest for practical applications.

[6] The energetic character of seismic noise in the double-frequency band leads to relatively large signal-to-noise ratios of correlation functions utilized in noise-based imaging and monitoring applications. In practice, correlation functions are imperfect reconstructions of the targeted interstation Green's function, which can be recovered from an isotropic, equipartitioned wavefield [e.g., *Campillo*, 2006]. Arrival time estimates of correlations constructed from anisotropic wavefields analyzed with crustal imaging techniques [e.g., *Shapiro and Campillo*, 2004; *Shapiro et al.*, 2005; *Sabra et al.*, 2005; *Yao et al.*, 2006; *Yang et al.*, 2008] are

therefore sensitive to the station orientation with respect to noise energy propagation [e.g., *Sabra et al.*, 2005; *Froment et al.*, 2010].

[7] The monitoring of subsurface velocity changes using noise techniques [*Wegler and Sens-Schönfelder*, 2007; *Brenguier et al.*, 2008; *Meier et al.*, 2010] can also be biased by variations in the excitation pattern. The coupling to atmospheric processes results in systematic seasonal variations of microseism properties, including amplitudes, frequency content, and composition and polarization of the wavefield [e.g., *Haubrich and McCamy*, 1969; *Schulte-Pelkum et al.*, 2004; *Roux et al.*, 2005; *Stehly et al.*, 2006; *Tanimoto et al.*, 2006; *Gerstoft et al.*, 2008; *Koper and de Foy*, 2008; *Koper et al.*, 2009; *Stutzmann et al.*, 2009; *Zhang et al.*, 2009; *Landès et al.*, 2010; *Schimmel et al.*, 2011]. A relevant improvement in the accuracy and reliability of noise-based imaging and monitoring results will be achieved by refined estimates about the spatiotemporal excitation evolution during an observation period.

[8] Here we report on progress in providing estimates for microseism source patterns. We investigate the relative match between excitation distributions obtained with an observational and modeling approach. Patterns of global microseism sources observed by *Landès et al.* [2010] between July 2000 and June 2001 are systematically compared with predictions obtained by sea state modeling coupled to microseism excitation theory. Our modeling extends the first-time application by *Kedar et al.* [2008] to the global scale. The parametrization of oceanic excitation mechanisms constitute an improvement compared to significant wave height patterns previously interpreted as proxies for microseism sources [*Gerstoft et al.*, 2008; *Stutzmann et al.*, 2009]. The general agreement between first-order properties of activity patterns of the two data sets serves as additional confirmation of the open ocean excitation hypothesis. Our results will help to calibrate theoretical approaches and to improve our ability to quantitatively describe the space-time variability of the ambient microseism wavefield.

2. The Data Sets

[9] We begin by introducing the observational and modeling techniques that result in the two data sets of global oceanic microseism activity patterns compared in this study. Details are given in the corresponding publications [*Landès et al.*, 2010; *Kedar et al.*, 2008] (hereafter referred to as L10 and K08, respectively). Here we discuss aspects relevant for our analysis. Hereafter "observations" refers to locations obtained after the processing and analyzing of seismological data; "modeled" and "predicted" locations are used in the context of wave action models (WAMs) coupled to excitation theory; "energy" is loosely used to address the excitation strength determined by each method; and "source" refers to above average microseism excitation.

2.1. Seismological Observations

[10] L10 analyzed data recorded between July 2000 and June 2001 at three arrays located in the United States, Turkey, and Kyrgyzstan in the double-frequency band, f_s = 0.1–0.3 Hz, with f_s denoting seismic wave frequency. Vertical component correlation functions are constructed from 13 days of continuous records, advancing by 3 day intervals. Using each of the networks as an array, correlations are used in a beam-forming analysis to locate sources associated with the targeted teleseismic phases. In the words of L10 (paragraph 19), this yields a 13 day averaged "characterization of the signal amplitude in the horizontal slowness domain," named A. Source locations are estimated by back projecting the slowness map results onto a global 2.5° latitude × 5° longitude geographical grid. This is achieved by applying ray tracing in a spherically symmetric Earth model, projecting the maximum "energy" at a given azimuth and slowness to each grid point consistent with the considered phases. L10 favored direct and refracted waves over diffracted and reflected waves, respectively, and thus focused on *P*, *PP*, *PKP*, *PKiKP*, and *PKIKP* phases. At each grid point, individual values from the three arrays are multiplied, and the resulting product was interpreted as probability of microseism excitation during the considered period.

[11] The underlying A values in the slowness maps constructed from correlations reflect the coherent phase energy associated with a given direction. Correlation amplitudes are sensitive to, and thus representative of, the amplitude of the signal that emanates from individual source areas. We therefore consider it adequate to interpret the resulting overall probability as a proxy to energy and continue to label it A. The slowness map energy was not, however, distance- or phase-corrected by L10 during back projection. This introduces a bias in the final microseism excitation estimates; that is, A is underestimated in regions associated with stronger attenuated phases. The P wave arrival

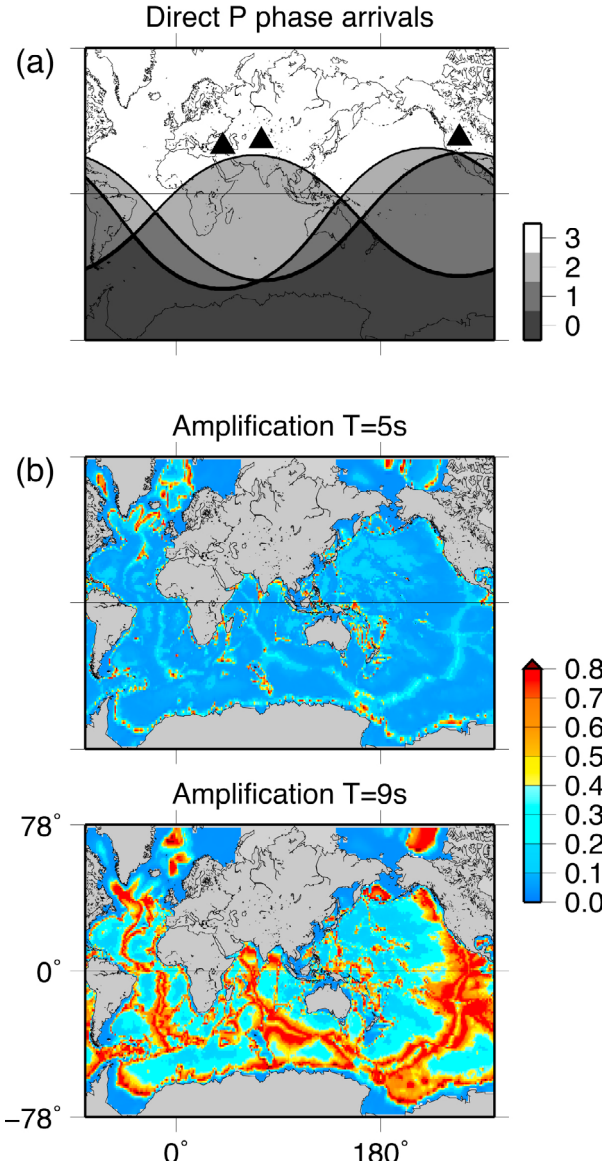

Figure 1. (a) The distribution of *P* wave shadow zones is a proxy for the attenuation effect. The grey scale indicates the number of networks that are reached from each location with a direct *P* wave (source-network distances within Δ = 104°). (b) Areas associated with large bathymetry-dependent amplification factors of wave-wave interaction intensities, $\sum_{m=1}^{3} c_m$ [*Longuet-Higgins*, 1950], are likely locations of effective microseism excitation. The two periods refer to seismic waves.

pattern in Figure 1a is used as a representation of the distance dependence throughout the study, although all of the five phases discussed above were considered by L10.

[12] The resolution limit to detect simultaneously acting sources can be approximated to the first order by estimates of the intensity pattern width associated with a point source. This is proportional to $\lambda\Delta/D$, the product of wavelength and source array distance over the dimension of the array. Then, two localized sources cannot be distinguished if they are closer than this distance. Using λ = 40 km, $\Delta = 10^3$ and 10^4 km, and D = 400 km, the lower limits of this estimate vary between 10^2 and 10^3 km, respectively. In practice, these estimates are modulated by the multiplication of three individual estimates that are obtained with three different resolution limits for a global source distribution.

2.2. Wave Action Models Coupled to Excitation Theory

[13] To estimate the energy transmitted into the seafloor as a result of atmosphere-ocean interactions, we extend the approach of K08 to the global scale. Hindcast sea state observations are coupled to the microseism excitation theory of *Longuet-Higgins* [1950] that considers the compressibility of the water column. Subsequent extensions of the theory that are not applied here considered random water waves [*Hasselmann*, 1963] and waves at shallow depths [*Webb*, 2007] and lower frequencies [*Tanimoto*, 2010]. These mechanisms do not influence excitation in the double-frequency band, and are thus considered to not affect our results. We compute directional spectral density functions F of wave-wave interaction intensities using the NOAA WAVEWATCH III (version 2.22; WW3) third-generation WAM [*Tolman*, 1999, 2005]. The wave model was driven with 6-hourly near-surface winds from the analysis product from the NOAA operational global assimilation and forecast system. The model state variable, i.e., the directional spectral density $F(f_o, \theta)$, in units of m^2 Hz^{-1} rad^{-1}, is a function of the ocean gravity wave frequency and the propagation azimuth, f_o and θ, respectively. The WW3 results cover 78°N to 78°S with a spatial resolution of 1° × 1.25° latitude-longitude, a directional resolution of 15°, and 25 logarithmically spaced frequency bands between 0.362 and 0.037 Hz (3.3 to 27.2 s). Sea ice data were taken from the NOAA assimilation system archives. Output was extracted from the model at 3 h intervals. The computation of simulated microseism generation using the wave model results F follows K08. The total wave-wave interaction intensities Ψ are calculated using

$$\Psi = \int_{f_o^a}^{f_o^b} \Omega(f_o)^{-1} \int_0^{\pi} F(f_o, \theta) F(f_o, \theta + \pi) d\theta \, df_o, \qquad (1)$$

where $\Omega(f_o)$ is the area of the directional spectrum bins in wave number space (m^{-2}; these are equal for a given wave frequency). In equation (1), only the waves traveling in opposite directions with the same frequency will contribute to the integral, in contrast to general estimates of sea state excitement parameterized by the significant wave height $H_s = 4\left[\int_0^\infty \int_0^{2\pi} F(f_o,\theta) d\theta df\right]^{1/2}$ [e.g., *Waxler and Gilbert*, 2006]. The computationally more efficient 15° directional resolution was selected after comparisons with results using more expensive 5° resolution. The two showed good agreement, though details for individual events did show some differences. In equation (1), the frequency integration limits f_o^a, f_o^b correspond to the frequency range $f_o = 0.05$–0.15 Hz and thus to seismic wave periods between 3 and 10 s after frequency doubling.

[14] The fluctuations described by Ψ correspond to simultaneously acting pressure changes at the base of the gravity layer, which "can be considered to be applied in the mean free surface" [*Longuet-Higgins*, 1953, p. 82] at $h = 0$. In this layer, the compressibility of water can be neglected, since the time for a pressure change to propagate downward is negligible. *Longuet-Higgins* [1950] estimated the depth extension of the gravity layer to be of the order of $1/2\lambda_g$, where λ_g is the wavelength of the causative ocean gravity wave. For 10 s period waves, λ_g/λ_c is of the order of 10^{-2}, where λ_c denotes the compressible wavelength. *Longuet-Higgins* [1950] further showed that resonance in the compressible layer below sustains unattenuated pressure oscillations in the water column, in contrast to exponentially decaying first-order fluctuations associated with particle motion. This "organ pipe effect" [*Longuet-Higgins*, 1953] is considered by applying a depth-dependent modulation of Ψ to estimate

$$\Psi_c = \Psi \sum_{m=1}^{3} c_m^2. \quad (2)$$

This yields a measure of energy flux into the solid Earth. The amplification functions c_m depend on the compressible wave frequency, which is equal to the excited seismic wave frequency $f_s = 2f_o$, the water depth h, and the elastic properties of the fluid and the underlying medium. Within the 1-D resonance case, the three gravest functions correspond to waves with no, one, and two nodal planes between the surface and the ocean bottom [*Longuet-Higgins*, 1953]. For the first wave, c_1 increases from about 0.2 (the transmission coefficient for the fluid-solid boundary) at $h = 0$ to 0.9 when h is about one quarter of the wavelength of a compression wave in water [*Longuet-Higgins*, 1950]. The spatial distribution of the frequency-dependent amplification factors are estimated from the ETOPO2 bathymetry data [*Smith and Sandwell*, 1997] (Figure 1b).

2.3. Adjusting the Data Sets for Comparison

[15] To make the two data sets spatially and temporally comparable, the seismological back projections are first up sampled to the denser WAM grid. We then take the mean Ψ_c value at each grid point from the $13 \times 24/3 = 104$ values computed in each observational period. This follows from the linearity of the correlation function. The correlation of any 13 day seismogram is equal to the stacked correlations obtained from the consecutive 104 three hour subseismograms. Hence, a short, strong source leaves the same footprint compared to a longer, yet weaker source that acts consistently at the same location. Areas from our comparative analysis that are covered by sea ice are excluded, using monthly average sea ice observations [*Meier et al.*, 2005; http://nsidc.org/data/docs/noaa/g02135_seaice_index]. The resulting two data sets consist of 113 frames of 288×157 grid points, centered at 5 July 2000 to 6 June 2001 in 3 day sampling intervals, covering ± 6 days.

[16] The values of observed source strengths A range between 10^{-6} and 1, with the lower limit chosen by the format precision. Note that the final value corresponds to the integration of a signal envelope that results from time-shifted cross correlations across a network (section 2.1 in L10). Hence, if no source is acting at a given slowness, the envelope of a random signal is integrated, and the resulting small, albeit nonzero, value is assigned to a location. Values close to 1 imply a very high degree of coherent energy observed at all networks. Peak values are found to not exceed 0.8, which corresponds to an average network coherence of 0.93. The modeled wave-wave interaction intensities Ψ_c are in units of m^6. Values range from 10^{-6} to several hundred, with peak values exceeding 10^3 m^6 during strong storms in the North Atlantic. The average source strengths for global A, Ψ_c distributions are $O(10^{-3})$, $O(1)$, respectively.

[17] Visual inspection of example distributions on the NH shows that predicted sources Ψ_c are well approximated by seismological observations A (Figures 2a and 2b). This can be inferred from the locations of the center of the excitation patterns in

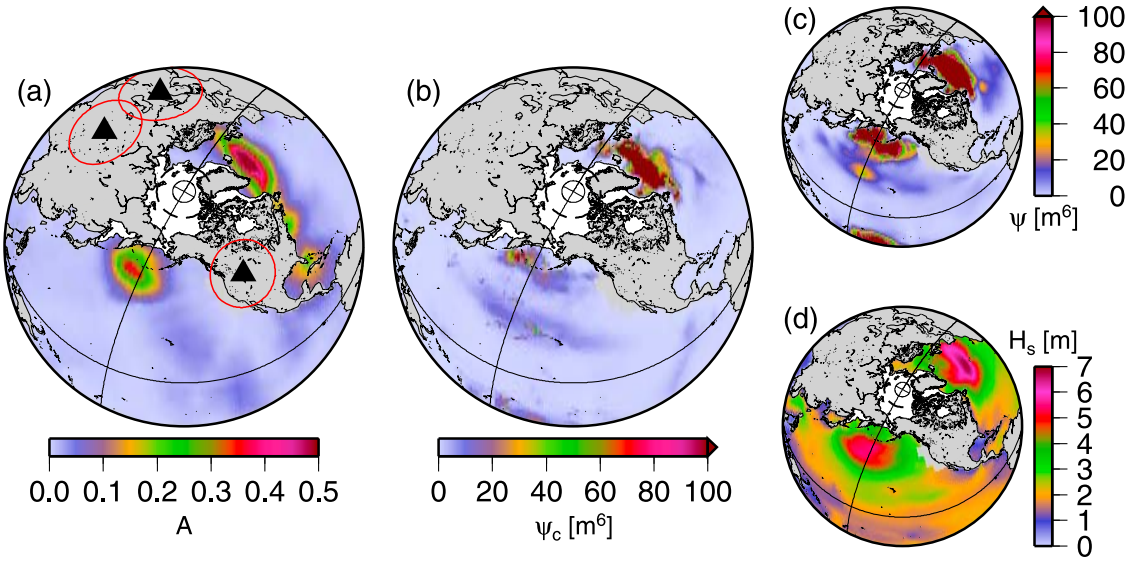

Figure 2. An example microseism excitation pattern of a 13 day observation window centered on 8 December 2000. (a) Seismological observations, A. (b) Wave-wave interaction modulated by bathymetry, Ψ_c. (c) Original wave-wave interaction Ψ, not modulated by bathymetry. (d) Significant wave height, H_s. Here and in all subsequent maps, white areas denote monthly averaged sea ice coverage, the dashed circle depicts the boundary of the modeling domain (78°N to 78°S), and red circles delineate the minimum back projection range (15°) around each network.

the North Pacific. In the example discussed in Figure 2 the A and Ψ_c foci are consistently located at longitudes <180°, whereas the Ψ and H_s distributions (Figures 2c and 2d) extend farther east. The qualitatively better agreement between A and Ψ_c compared to Ψ indicates the relevance of the organ pipe effect. The extended source in the North Atlantic allows no inference about the resonance effect that differentiates the hindcast-based Ψ_c and Ψ distributions (equation (2)). In contrast, the H_s center of activity is located farther south compared to regions of maximum Ψ, Ψ_c, and A estimates. This indicates that wave height estimates, although easier derived from directional spectra F, are not reliable proxies of microseism generation (see also Figure 2b of K08).

[18] To facilitate a systematic comparison between A and Ψ_c across several orders of magnitude, values of both data sets are converted to decibel, using $A^{\mathrm{dB}} = 10\ \log_{10}(A/10^{-6})$ and $\Psi_c^{\mathrm{dB}} = 10\ \log_{10}(\Psi_c/10^{-6}\mathrm{m}^6)$, respectively. As discussed in section 3, the common 10^{-6} lower cutoff value results in a limited bandwidth for below average values of the observational approach. Finally, A^{dB}, Ψ_c^{dB} values in each frame are scaled using $A^* = A^{\mathrm{dB}}/\langle A^{\mathrm{dB}}\rangle$ and $\Psi_c^* = \Psi_c^{\mathrm{dB}}/\langle\Psi_c^{\mathrm{dB}}\rangle$, where $\langle\cdot\rangle$ denotes the mean value of the associated global energy distribution. This way, increased (>1) and decreased (<1) A^*, Ψ_c^* values indicate regions of microseism excitation above and below the global average. It is important to note that before the distribution mean is estimated, the data sets are scaled by the latitude-dependent grid segment area. Hence, sources at high latitudes have a smaller impact on the global distribution.

2.4. Resolution and Target of the Analysis

[19] The mapping $[A, \Psi_c] \rightarrow [A^{\mathrm{dB}}, \Psi_c^{\mathrm{dB}}] \rightarrow [A^*, \Psi_c^*]$ de-emphasizes inaccuracies associated with a potentially fuzzy resolution of intermittent, strong, localized predictions. Better agreement is consequently achieved between observed and predicted distributions over broader regions with similar (scaled) energies. The sensitivity of the analyzed spatial coherence is thus steered to first-order effects, e.g., hemispheric patterns and the relative contributions from coastal or pelagic areas. However, the applied scaling does not remove the systematic underestimation of excitation amplitudes remote from the networks.

[20] As a result of the missing distance or phase correction, the spatial distribution of the arrays emphasizes amplitudes on the NH (Figure 1a). Consequently, the resolution, i.e., the gradient between above and below average excitation states,

is larger. In contrast, large areas on the Southern Hemisphere (SH) do not emit direct *P* phases that are observable by at least one or two networks. This leads to a mapping of underestimated source strengths to these regions, which also affects the mean of the global A^{dB} distribution. This inconsistency cannot be fixed in retrospect since the contributions of each individual network to the final *A* value of a grid point are not available. However, the distorting effect is limited by the latitude-dependent scaling, which mostly affects the remotest areas located at relatively high latitudes on the SH. In addition to the impact of attenuation on the signal quality, the angular resolution of the network configuration controls the spatial sensitivities. This was not, however, systematically tested. We expect that a solely acting unit source in close proximity to all three networks will be better resolved spatially, both in amplitude and space, compared to an equal source acting at great distance. The associated bias is likely amplified by the use of a 1-D Earth model during the back projection and the accumulation of errors along long travel paths of weak amplitude phases. We discuss some case studies in section 5.1.

[21] Predicted source strengths are also not homogeneously distributed. According to theory, the spatial distribution of microseism excitation is expected to reflect ocean depth. The translation of global bathymetry data into maps of peak resonance values identifies likely source regions of strong secondary microseism excitation in the event of first-order wave-wave pressure oscillations (Figure 1b). For the seismic frequency range between 0.1–0.3 Hz, these regions correspond to water depths between about 3800 and 2000 m, respectively. Laterally connected regions in this depth range are found predominantly along mid-ocean ridges and on continental slopes.

[22] The aim of this study is twofold. First, we assess the global microseism activity pattern and the associated spatiotemporal variations. For this we consider the WAM predictions equally relevant compared to the seismological observations. We decide to discuss the results of the global comparison and to not limit our analysis to areas that are least affected by attenuation (white area in Figure 1a). To demonstrate the implications of an alternative approach, we present one of our key results processed exclusively for the limited area defined by the best direct *P* wave coverage (section 4.3). We find that our main conclusions do not need to be modified. Implications of the missing amplitude corrections are discussed with each analysis. Second we compare the data sets to identify robust features in both distributions. Simultaneously, consistent mismatches between observed and modeled microseism source estimates indicate systematic sensitivity variations. They mainly depend on specific processing details that are relevant for the construction of each data set.

3. Temporal Evolution of Excitation Patterns

[23] We analyze the temporal evolution of spatially independent A^{dB} and Ψ_c^{dB} excitation patterns. For this, we divide the global distributions into subsets associated with the NH and SH, respectively. We find a distinct polarity change in the differential patterns of the microseism excitation distributions (Figures 3a and 3b). The overall similarity between the observed and predicted patterns suggests the adequate registration of seasonality by both approaches. The most significant difference is identified during NH spring (around January 2004). Observed A^{dB} distributions are dominated by NH excitation patterns whereas the inverse relationship governs modeled Ψ_c^{dB} distributions. This is attributed to the attenuation bias. High-energy states on the SH are underestimated, and the differential pattern is therefore dominated by the larger NH states.

[24] Considering the hemispheric A^{dB} and Ψ_c^{dB} distributions individually (Figures 3c–3f), we find that histograms of observed A^{dB} have a narrow range of sizes compared to Ψ_c^{dB} associated with the WAM predictions. The difference arises from the common lowest value, and the limited observation range $A < 1$, compared to peak Ψ_c values exceeding 10^3 m^6. This is synonymous with a reduced bandwidth of the observational approach that cannot image the spectrum of synthetic source strengths. The A^{dB} distributions on the NH become positive skewed during the respective winter months (Figure 3c). For the SH results the skewness is evident yet less distinct during SH winter, a consequence of the amplitude mapping (Figures 3c and 3e). In other words, the seismological analysis indicates the occupation of higher energy values ($A^{dB} > 45$ dB) during the winter months on each hemisphere (Figures 3b and 3c). This is consistent with previously observed seasonal changes in the properties of ambient noise in the microseism frequency band [*Stehly et al.*, 2006; *Tanimoto et al.*, 2006; *Gerstoft et al.*, 2008; *Koper et al.*, 2009; *Stutzmann et al.*, 2009; *Schimmel et al.*, 2011]. The corresponding differential pattern demonstrates that the network distribution qualitatively resolves

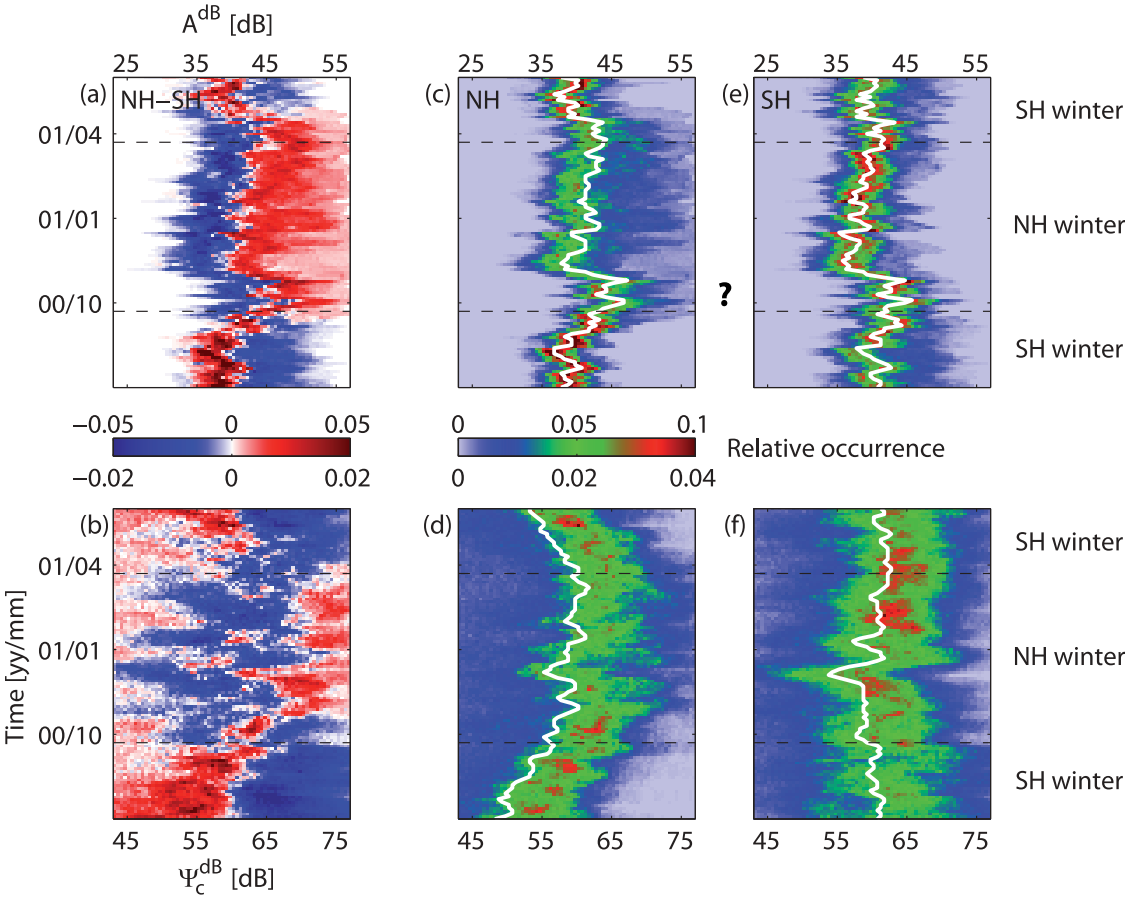

Figure 3. Temporal analysis of (top) observed and (bottom) modeled scaled energy distributions reveals fundamental properties of hemispheric microseism evolution. Time runs from bottom to top. A horizontal slice, advancing in 3 day intervals, represents a histogram of A^{dB}, Ψ_c^{dB} values. Colors illustrate the height of the histograms, and the white lines mark the hemispheric distribution mean in each frame. Dashed lines indicate autumnal and vernal equinox. Observed and predicted (a and b) hemispheric differential pattern and (c and d) NH and (e and f) SH distributions. Note the increased energy states (long tails) during respective winter months in Figures 3c–3f. Similarly, distributions are narrower during summer months, indicated by the red peak pattern. The question mark between Figures 3c and 3e indicates a period of observed increased global energy during NH fall 2000, which is not paralleled by a hindcast-based quantity (H_s, Ψ, Ψ_c). The signal does also not correspond to a diagnostic network operation status.

global trends in microseism excitation, despite their concentration on the NH.

[25] Model distributions of Ψ_c^{dB} have a systematic negative skew (Figures 3d and 3f). It reflects the large range of size scales and that large excitation states are limited to few sites. In contrast to the relatively constant mean observed energy, the "curved" shape of the modeled energy evolution on the NH suggests a significant seasonal variability (Figure 3d). The pattern for the SH shows only a very weak inverse trend. Together with the corresponding differential pattern this behavior implies that the annual variation of pelagic microseism generation on the SH has a much lower amplitude than on the NH. Seasonality in the global signal largely reflects the dominance of the NH signals during the boreal winter. This difference in the modeled seasonality between the two hemispheres can be understood by the combination of not parameterized coastal processes and concentration of land on the NH. Missing coastal contributions emphasize the influence of offshore activity pattern. The lack of obstructing topography in the Southern Ocean allows the formation of atmospheric patterns at midlatitudes ("roaring forties," "furious fifties") that result in the relatively small annual variability of microseism excitation.

[26] This hypothesis is supported by the observations considering the similarity of the differential patterns. More data from the SH are needed to

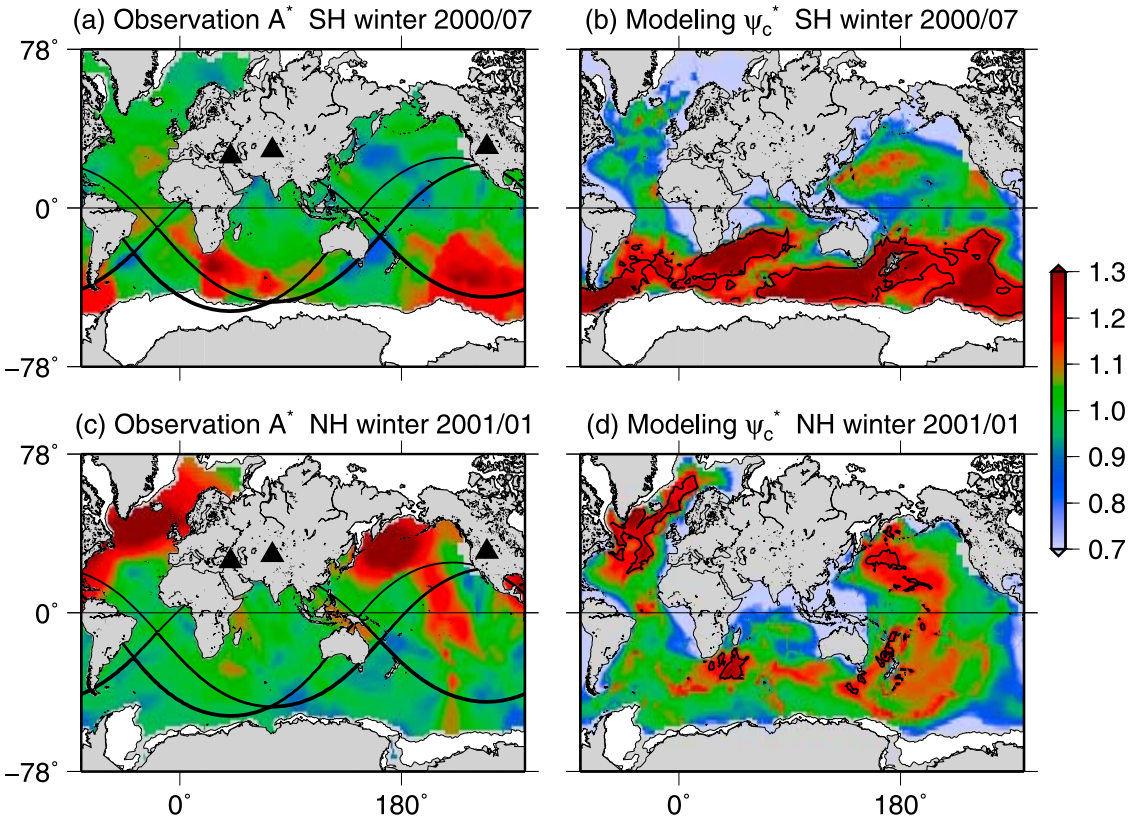

Figure 4. Maps show scaled monthly averaged excitation estimates, A^* and Ψ_c^*, for (a and b) SH and (c and d) NH winter months, respectively. Scaling to decibel results in a blurring effect in areas with relatively large amplitudes, which facilitates a pixel-by-pixel comparison of the two data sets by averaging localized predicted sources (section 5.1). Here and in Figures 5, 7, and 10, the three lines indicate the *P* wave boundaries (Figure 1a). Note the reduced A^* amplitudes south of these boundaries (Figures 4a and 4c) and the overall low predicted Ψ_c^* values near coastlines (Figures 4b and 4d). Contours in Figures 4b and 4d highlight strong open ocean sources (compare to Figure 5).

further analyze systematic differences between NH and SH excitation.

4. Spatial Distributions of Excitation States

4.1. Scaled Energy

[27] A comparison of energies scaled to the global average, A^* and Ψ_c^*, stacked over a SH (July 2000) and a NH (January 2001) winter month adds spatial information to the patterns discussed in section 3. The previously discussed range of size scales are reflected by the different distributions of color in Figure 4. That is, observed patterns are dominated by average values, and few areas show distinctive deviations from the mean. Maps of Ψ_c^* on the other hand are more nuanced, with larger gradients between above and below average source strengths.

[28] During SH winter (Figures 4a and 4b) the observations do identify areas of increased A^* on the SH. The corresponding Ψ_c^* distribution is characterized by increased excitation states throughout much of the SH, average pelagic excitation on the NH, and low estimates around coastlines. Systematic mismatches between the A^* and Ψ_c^* distributions are low coastal Ψ_c^* values, and open ocean A^* lows in areas of Ψ_c^* highs. The two low-A^* regions on the SH are biased by the attenuation effect, since they are located in regions from which no direct *P* wave can reach any of the networks. Predictions indicate a broad region of elevated values across the western subtropical Pacific, coincident with the southern flank of the mean summer cyclone track that leads to high original Ψ estimates [*Zhang et al.*, 2010; *Mesquita et al.*, 2010]. As coherent energy from fast moving, localized depressions cannot be resolved by 13 day averaging periods, this feature is not apparent in the observations. Alternatively, slightly above average Ψ_c^* estimates in this region is possibly associated with values that are large relative to the low coastal estimates that bias the distribution mean.

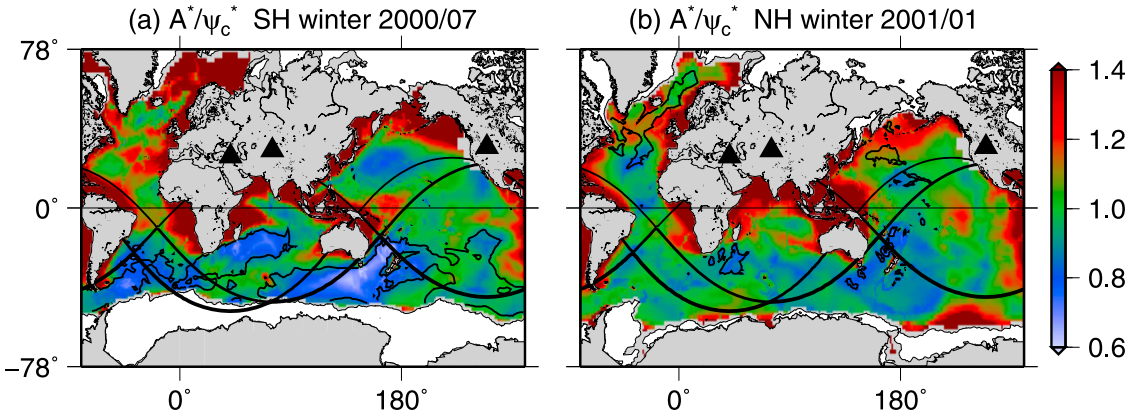

Figure 5. Ratios of A^*/Ψ_c^* from Figure 4 assess the relative coherence during (a) SH and (b) NH winter months. Deep ocean sources in the direct shadow zone (Figure 4) are systematically underestimated by A^* due to missing amplitude corrections during back projection. Contours correspond to strong Ψ_c^* source estimates (compare to Figures 4b and 4d). Energy from coastal areas are globally underestimated by Ψ_c^*, since a parametrization of microseism generating near-coastal processes is not included in the WAM.

[29] During NH winter (Figures 4c and 4d), visual comparison of the A^* and Ψ_c^* maps suggest a coarse overall agreement in the distribution of increased excitation states on the NH, which concentrate in the northern Atlantic and Pacific Oceans. The networks map similar scaled amplitudes to the Atlantic and Pacific sources, in contrast to ocean state modeling, which predicts stronger sources in the Atlantic due to resonant water depths (compare with Figure 1b). As for the SH winter case, Ψ_c^* distributions are characterized by low coastal values. Despite the positions of the networks the predicted source south of Madagascar is identified with an $A^* > 1$ intensity, suggesting that this area is a hot spot for microseism excitation.

4.2. Relative Match

[30] We plot the relative match between the two data sets by taking the ratio of the two scaled distributions, A^*/Ψ_c^* (Figure 5). The resulting maps highlight the quantitative differences between the two approaches, and constitute a key result of our analysis. In particular, values >1 (red; relatively more energy observed than modeled) are concentrated mainly around coastlines. This result is universal, i.e., insensitive to observation period and considered region; it reflects the lack of parametrization of near-coastal processes in the generation of the synthetics. Values <1 (blue; relatively less energy observed than modeled) are mostly observed on the SH. This trend, which is more pronounced during the SH winter, is testament to the decreased amplitude estimates at the larger distances from the arrays. Smallest ratios are observed south of regions from which direct P waves can be observed by any one network. Recalling that the direct P wave horizons were introduced as a proxy for the attenuation effect, we find that this parametrization has an adequate explanatory power. How sensitive is this key result to the attenuation bias? Section 4.3 presents an illustration of a simplified version of Figure 5 that visualizes the effect. Here, we briefly report on the results of an analysis exclusively applied to the white area in Figure 1a. We find no significant distortion of the pattern in Figure 5. Small changes associated with the redistributions of values as a consequence of the neglect of the entire SH and much of the Indian and Pacific Oceans mainly emphasize nuances in the Atlantic during SH winter. That is, the ratio A^*/Ψ_c^* becomes more negative south of Iceland, or west of Africa. During NH winter, no differences can be detected.

4.3. Binary Comparison

[31] It is useful to assess the match in terms of increased and decreased energy. While the A^*/Ψ_c^* ratio yields a measure of the relative size of the two scaled energy estimates, it introduces a bias that is associated with the different range of size scales. Consider the area south of Madagascar during NH winter (Figures 4 and 5): both the scaled observations and the predictions identify increased energies relative to the respective global mean of the corresponding monthly analysis period (red, with different intensities, in Figure 4). However, predicted values ($\Psi_c^* \approx 1.25$) are larger than observed values ($A^* \approx 1.1$), which gives a ratio $A^*/\Psi_c^* < 1$ for this

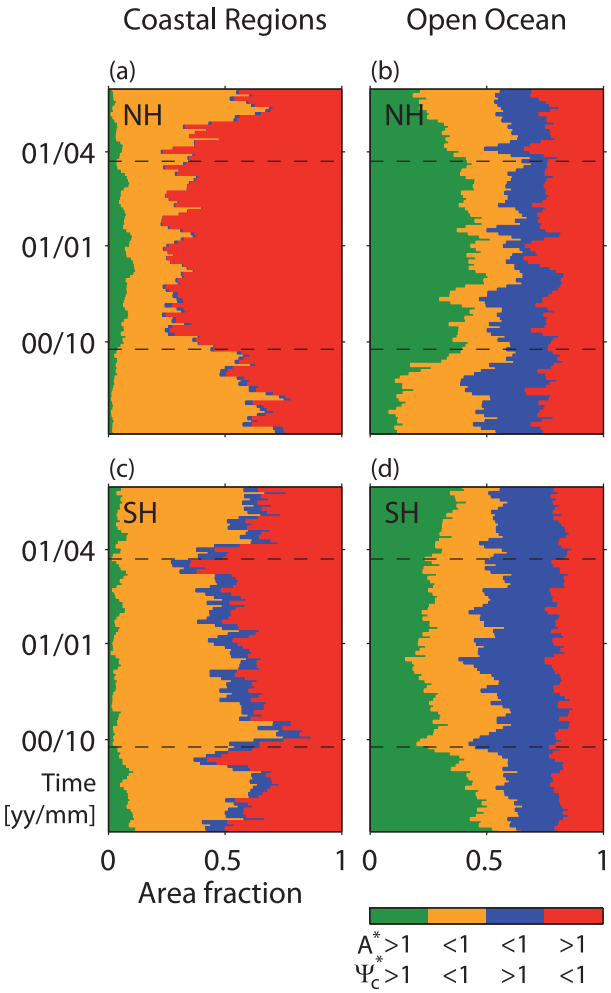

Figure 6. The temporal evolution of the relative coherence between A^* and Ψ_c^* is analyzed applying a "binary" measure (section 4.3). We separate between (a and c) coastal regions, defined by an area within 3° of mapped coastlines (i.e., 3 pixels wide) and (b and d) offshore regions. Time runs from bottom to top, and each horizontal slice, advancing in 3 day intervals, corresponds to one observational period. The dashed lines indicate autumnal and vernal equinox. Red sections indicate the relative area size in which increased energy is observed but decreased energy is modeled, while blue sections indicate the opposite. Recall that increased and decreased energies are measured with respect to the mean of a frame's global A^{dB} and Ψ_c^{dB} distribution. Green and orange sections indicate that a pixel is occupied by both increased and decreased A^* and Ψ_c^* values, respectively.

particular region (Figure 5). By determining whether the values at each pixel agree with respect to the global average estimate, we arrive at distributions that consist of the four possible combinations of increased and decreased modeled and observed values, respectively (Figures 6 and 7).

[32] Following the results obtained in section 4.2, we distinguish between coastal regions (pixels within a 3° radius around the coastlines) and offshore regions.

[33] On the NH, the largest discrepancy is the observed excess energy that arrives from coastal areas during the NH winter (Figure 6a, red). This mismatch is much lower for offshore areas (Figure 6b, red). About 15–20% of the predicted increased offshore energy states have a below average value in the observational distributions (Figure 6b, blue). This is likely attributed to the "masking" effects of the above average coastal estimates. It causes moderate excitation states to appear below average, a feature that is revisited in section 5.2.

[34] Near-coastal energies during the NH summer (Figure 6a, orange) are consistently below average, and active offshore sources during the NH winter (Figure 6b, green) are above average.

[35] The results for the SH are qualitatively similar, albeit seasonally inverted. Coastal areas are dominated by excess observed, but not modeled, source strengths (Figure 6c, red). The resulting offshore masking effect appears somewhat larger compared to the NH (Figure 6c, blue). There is agreement on the decreased coastal energies during the SH summer (Figure 6c, orange), and on the increased offshore energies during the SH winter (Figure 6d, green).

[36] These results also justify the analysis of the global data sets, since the significance of the coastal process has also been demonstrated on the SH, and matches concerning the pelagic pattern are only slightly lower compared to the NH (sum of green, yellow segments in Figures 6b and 6d). Yet, how does attenuation bias this result? We examine patterns similar to Figures 6a and 6b constructed exclusively for the best resolved area on the NH (not shown). We find no temporal evolution of the coastal pattern, and the small inverse seasonality of the yellow and blue pattern in open ocean areas does not provide additional information over the presented evolution of the global results.

[37] Figure 7 is complementary to Figures 6 and 4. While Figures 7a and 7b present the results of the global analysis, Figures 7c and 7d are limited to the observationally best covered areas. We conclude that the binary maps contain significantly refined results over the A^*/Ψ_c^* patterns in Figure 6. During SH winter, much of the predicted increased excitation states on the SH are confirmed by the array

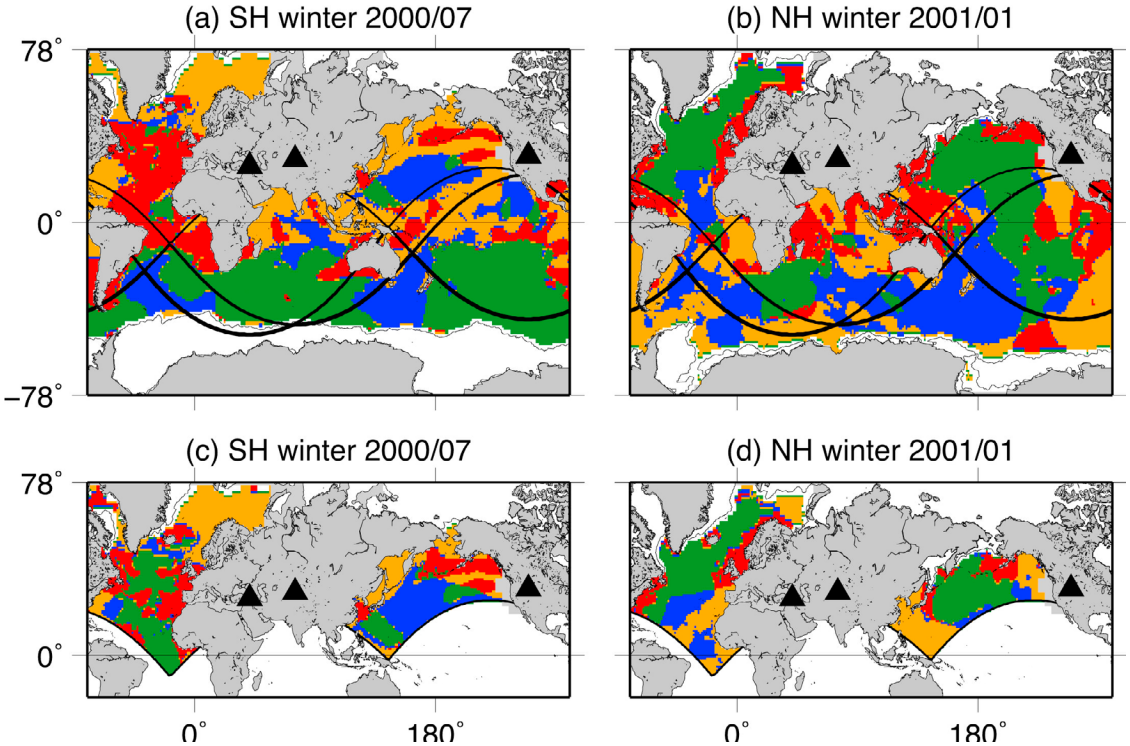

Figure 7. We analyze the spatial binary mapping for (a) a SH winter episode and (b) a NH winter episode. The same color scheme as in Figure 6 applies. We find overall higher similarities between the two estimates compared to the results in Figure 5. (c and d) Distributions showing the results of an alternative approach in which only areas with the best observational coverage are considered.

processing. Exceptions are limited to blind spots at maximum distance to the networks. As a consequence, sources in the Atlantic are overestimated. During NH winter, pelagic excitation states agree well on the NH, and on the SH the persistent source off South Africa is resolved. Discrepancies arise mainly along coastlines in response to the missing parametrization in the WAM models. Modifications of these conclusions from targeting the best resolved areas (Figures 7c and 7d) consist of an improvement in the relative matches in the Atlantic and western Pacific during SH and NH winter, respectively.

5. Assessing the (Mis)Match Between Observations and Predictions

[38] So far our analysis indicates a match in the seasonal variability of observed and modeled excitation states. In addition to the previously discussed sources in the North Atlantic, several comparisons substantiate the identification of at least one excitation hot spot on the SH southeast of South Africa. Mismatches occur systematically along coastlines, where microseism excitation is not parameterized, and on SH offshore areas, where attenuation effects result in underestimated observed amplitudes. In this section, we compare individual, i.e., spatio-temporally confined, microseism sources.

5.1. Open Ocean

[39] For individual frames, we select geographically confined areas during both hemispheric winters that contain strong observed and predicted excitations (Figures 8a–8c). Here, we discuss original A and Ψ_c values to demonstrate the effects more clearly and to be independent of the scaling operations.

[40] A typical pattern for strong microseism generation (peak $\Psi_c > 10^3$ m^6) in the North Atlantic during NH winter is an intense storm system that moves northeastward from off North America. The combination of high waves generated by southwesterly winds to the southeast of the center of the storm, and by northeasterly winds to the north, leads to intense wave-wave forcing in regions with depths that are favorable for efficient microseism generation (Figures 8a and 8b; see also Figure 2b in K08). Considering, for example, two observation periods centered on 1 and 10 January 2001 (Figures 8a

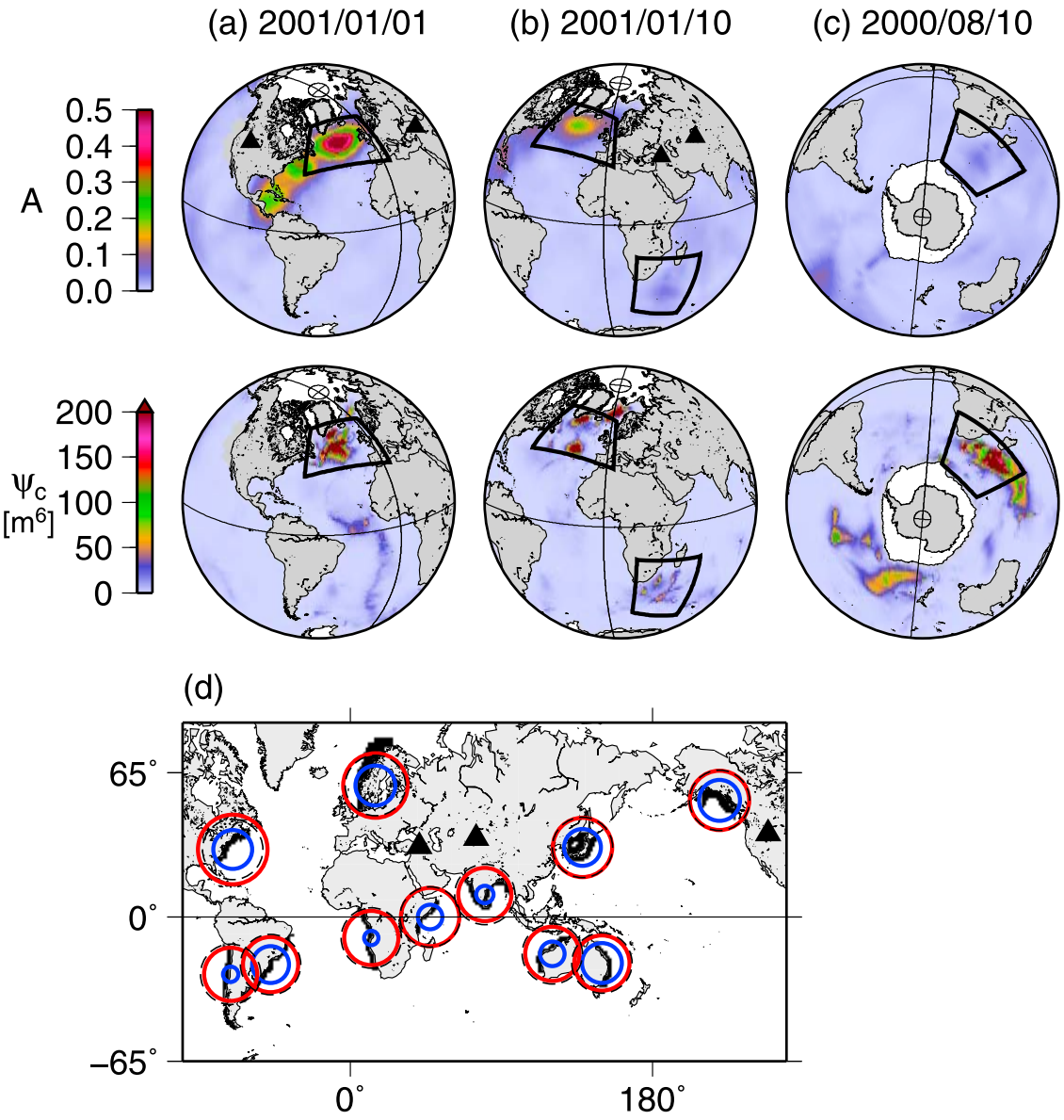

Figure 8. A comparison between observed and predicted open ocean and near-coastal excitation estimates assesses the mismatches between the two estimates. (a–c) Comparison of (top) observed (A) and (bottom) predicted (Ψ_c) values for selected offshore microseism excitation episodes. Unscaled values are used. Numbers discussed in the text are averages of high-amplitude values within the boxes. (d) Comparison of observed (A^*, red) and predicted (Ψ_c^*, blue) average near-coastal source strengths. Scaled values are used. The circle size corresponds to excitation strength. The dashed circles indicate the respective global average, i.e., $A^* = \Psi_c^* = 1$. Selected coastal areas are indicated in black (3 pixels wide).

and 8b). The mean modeled high-energy values south of Iceland are Ψ_c = 250 m^6 and 500 m^6, respectively, while observed estimates are in the range of A = 0.5 and 0.2, respectively. We note that during the first period (1 January, Figure 8a), no other activity with comparable strength was identified. During the second period (10 January, Figure 8b), a single source off Japan with peak Ψ_c = 400 m^6 was acting simultaneously (data not shown), which was assigned an even higher observed value, A = 0.3 (compare to off Iceland Ψ_c = 500 m^6, A = 0.2). The spatially averaged source south of Iceland is a consequence of the closely spaced, yet separated, individual sources acting simultaneously in this region.

[41] This example demonstrates the correspondence between the resolved wavefield coherence A and

the localization of the source. It also shows that the beam-forming approach can resolve multiple sources on the global scale (compare Figure 2) and shows the limitations in the angular resolution for a case of two collocated sources. Using $\lambda\Delta/D$ (section 2.1) with λ = 40 km, Δ = 4500 km (the average distance between the arrays and the center of the black rectangles on the NH in Figures 8a and 8b) and D = 400 km, we obtain a resolution limit of 450 km. Clearly, the sources in Figure 8b are separated by more than this limit, even when we assume somewhat larger phase velocities and distances along the refracted rays. Provided that the predictions are a reasonable approximation of the open ocean excitation, this indicates that the resolution limit of the beam form and back project approach falls below this estimate.

[42] A third, weaker, source south of Madagascar, with mean predicted values of Ψ_c = 40 m^6, yields an observed A = 0.04. A similar analysis for this source region in the Southern Ocean around 35°–55° longitude during SH winter source periods (e.g., 10 August 2000, Figure 8c) indicates that Ψ_c = 350 m^6 amplitudes are identified with A values that rarely exceed 0.1–0.2.

[43] To summarize, using values from both hemispheric winters, we find that a modeled Ψ_c = 250 m^6 source on the NH is seen with A = 0.5, while a source on the SH with Ψ_c = 350 m^6 is identified only with A = 0.1. Together, these examples emphasize the spatiotemporally varying ability of the networks to detect and resolve sources: (1) two simultaneously acting sources that are close together are mapped to an average location; (2) two simultaneously acting sources that are widely separated are assigned lower individual amplitudes, as compared to a solely acting source of similar strength; (3) weaker sources on the SH during NH winter can nevertheless be resolved; and (4) strong sources on the SH are assigned lower observed amplitudes compared to similar sources on the NH. Hence, mismatches between the two scaled data sets regarding open ocean source strength estimates are dominated by incorrect amplitude mapping during back projection and the angular resolution.

5.2. Coastal Areas

5.2.1. Global Examples

[44] We analyze the discrepancy in coastal areas. To compare regional differences to the global average, we switch back to the scaled values Ψ_c^*, A^*. We choose 11 coastal strips for which we determine the observed and modeled excitation estimates (Figure 8d).

[45] We find that the relative magnitudes of A^* and Ψ_c^* show considerable regional variability. This variability is more significant compared to a potential trend associated with the average network distance. Compared to the observed seasonal changes in offshore excitation, regionally only weakly increased A^* amplitudes are found during winter months. It indicates weaker seasonal excitation variations in coastal areas, as also noticed by *Schimmel et al.* [2011]. Predicted amplitudes for the northern midlatitudes coastlines show a more pronounced annual dependence. Such dependence is not observed for the coasts in equatorial regions or on the SH.

[46] In general, there is good relative agreement for the coastal regions off northern Europe, Alaska, eastern North America, eastern South America, and eastern Australia. In contrast, there is a significantly high coastal A^*/Ψ_c^* ratio off western South America and West and East Africa and around India. Considering the small variability in the average coastal A^* values, these results reflect a large range in overall below average Ψ_c^* values.

[47] Identification of the mechanisms responsible for the observed coastal excitation will improve our understanding of microseism generation and sources. Certainly, coastal reflections are important in favored regions, where large waves arrive from directions at least close to an approximate perpendicular to the coastline, and there is a lot of evidence for the regional importance of this mechanism [*Elgar et al.*, 1994; *Bromirski et al.*, 1999; *Schulte-Pelkum et al.*, 2004; *Tanimoto et al.*, 2006]. *Graham et al.* [2010] used mirror images of incoming swell spectra to study microseism excitation off the southern California coast. While the timing of the resulting synthetic onshore ground displacement was consistent with seismological observations, the amplitude differences highlighted the sensitivity of near-coastal processes to a multitude of factors. At the same time, open ocean (not involving reflections) wave-wave interaction mechanisms probably have some minor contributions to the nearshore waters as well. A third mechanism also appears to be at work, which does not involve opposing waves, at least in the sense described here. For example, *Zhang et al.* [2009] demonstrated strong coherence between fluctuations in wind speed off the California coast and microseism energy detected just inland. While most of their analysis focus on microseism energy at frequencies higher than considered here (0.6–2.0 Hz),

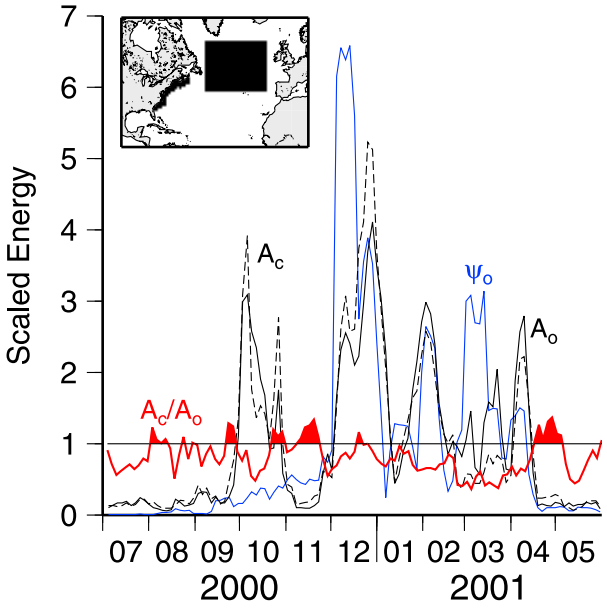

Figure 9. To study the relative contribution to observations, we analyze the temporal evolution of coastal (subscript *c*) and offshore (subscript *o*) energies. The time series represent excitation averages in the regions shown in the inset. To be comparable on the same scale, yet unaffected by the global excitation pattern, A_c (dashed black line), A_o (solid black line), and Ψ_o (blue line) are scaled by their temporal means. Observed coastal energy tends to exceed observed offshore energy ($A_c/A_o > 1$, red line) only at times of relatively calm offshore sea states, indicated by low A_o, Ψ_o values.

their findings clearly indicate excitation is occurring for short gravity waves in situations where wave direction should be quite uniform and more or less parallel to the orientation of the coast. It is plausible that, combined with depth dependence, this mechanism also contributes to the near-coastal energy seen in our observations.

[48] Note that $A^* > \Psi_c^*$ for coastal regions, with the inverse tendency $A^* < \Psi_c^*$ for open ocean regions (e.g., Figure 8b). Summarizing a range of individual source comparisons, we find that the degree of coastal overestimation (A^*/Ψ_c^*) is about 2 to 4 times larger compared to the open ocean mismatch (Ψ_c^*/A^*). This raises the question of the relative contributions to observations if both source mechanisms, coastal and open ocean, are acting simultaneously.

5.2.2. Case Study: Excitation in the North Atlantic

[49] To address this, we examine the consistently observed pattern of increased coastal energy along the North American east coast and offshore south of Greenland during NH winter (Figures 2c, 4, and 8a). Figure 9 explores the observed coastal source strength relative to the offshore activity for this region. Here, time series are scaled by their temporal means to be comparable on the same scale. The scaling is hence not biased by remote activity. We find that the observed coastal excitation closely follows the collocated observed offshore pattern ($A_c \approx A_o$; black lines in Figure 9). The observed activity patterns show a very good phase coherence with the modeled open ocean estimates (blue line). Discrepancies during NH winter months arise mainly in amplitude. This can be explained by the sensitivity of the observed energy to global activity patterns (section 5.1). The spurious peak in observed energy during October 2000 corresponds to the associated signal discussed in Figure 3. The relative measure, A_c/A_o (red line in Figure 9), indicates that contributions from coastal areas tend to dominate the observations only during relatively calm open ocean sea states, i.e., predominantly during SH winter.

[50] A similar excitation pattern along the east coast is resolved by analyses of microbarom signals [*Le Pichon et al.*, 2009; *Landès et al.*, 2011]. These observations depend on a much denser network distribution, thus minimizing the possibility of the signal being an artifact of seismic signal processing. The mechanism of this near-coastal excitation remains to be identified. In addition to the possibilities discussed above, we note that excitation possibly benefits from the amplifying depth regime associated with bathymetric contours of the continental slope between 30° and 45° latitude (Figure 1b).

6. Conclusions and Perspectives

[51] Our comparison of two independent estimates of microseism excitation patterns in the double-frequency band (0.1–0.3 Hz) between July 2000 and June 2001 confirms seismic wave excitation in the open oceans [*Longuet-Higgins*, 1950, 1953; *Cessaro*, 1994; *Kedar et al.*, 2008; *Kedar*, 2011]. We find that the observational approach of *Landès et al.* [2010] (the application of array techniques to correlation functions of ambient noise records) has an increased sensitivity to source locations approximated by the arrival range of direct *P* phases. The locations of the used arrays on the NH limit this area primarily to the NH. The modeling approach, satellite-based hindcast sea state observations coupled to excitation theory, has a spatially uniform resolution. It does not, however, provide realistic excitation estimates

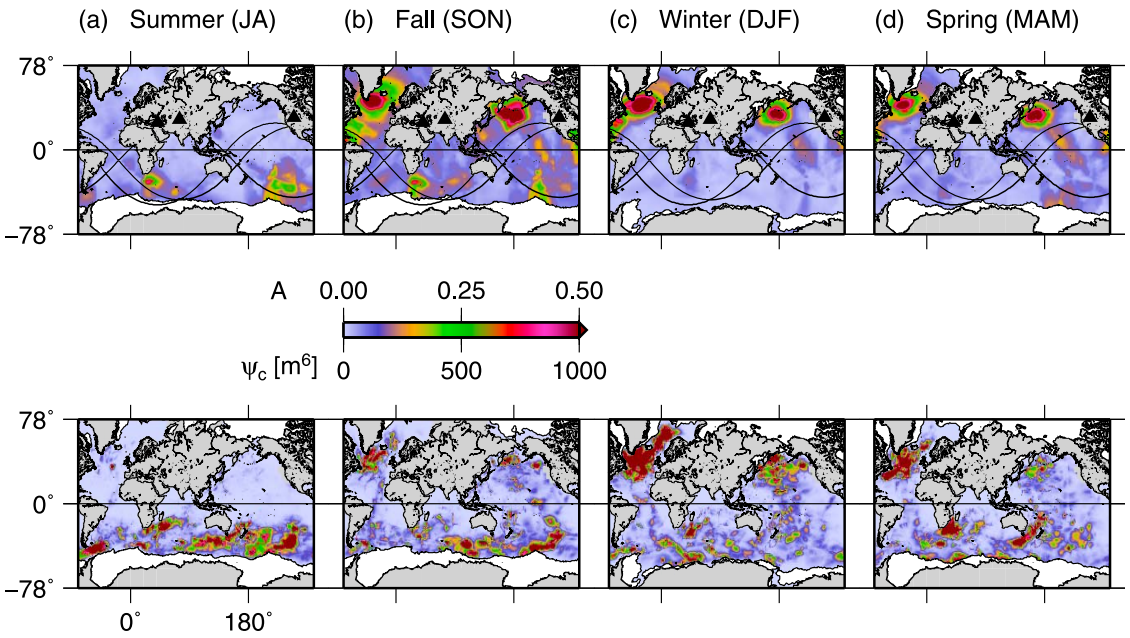

Figure 10. (top) The observed and (bottom) predicted global excitation patterns can serve as a template for future investigations of global microseism hot spot activity. Each pixel is occupied by the maximum A, Ψ_c value measured during the respective season. Seasons are associated with the NH. Letter combinations indicate months: JA, July, August; SON, September, October, November; DJF, December, January, February; and MAM, March, April, May.

in near-coastal seas. Absorbing boundary conditions prohibit coastal reflections that could interact with the incoming swell.

[52] Figure 10 provides the global distribution of the peak observed (A) and modeled estimates (Ψ_c) during the four seasons of the observation period. Maps of Ψ_c in particular predict localized hot spots. On the SH, distinct patches emerge to the south of South America, South Africa, and Madagascar, around the eastern and southern Australian coasts, and in the Southern Ocean around 220° longitude. On the NH, strong excitation regions are limited to the North Atlantic and Pacific Oceans. A comparison with Figure 1b reveals that excess open ocean microseism excitation is favored by regions with amplifying bathymetric conditions. An exception are the seas between Australia and New Zealand.

[53] Our systematic analysis of the spatiotemporal evolution of microseism patterns on the global scale and the associated discussion on (mis)matches between observed and modeled distributions allow the following conclusions.

[54] The temporal evolution of predicted and observed hemispheric differential excitation patterns agree on the seasonally dependent polarity change (Figure 3). This is because hemispheric distributions of both data sets consistently have long tails of increased energies during winter months. It indicates that the networks resolve annual hemispheric fluctuations, despite their inhomogeneous distribution and the missing amplitude corrections. In addition, the model approach suggests a relatively high, constant activity on the SH, which is dominated by the stronger activity on the NH during NH winter. A confirmation of this pattern depends on more observations of the microseism weather on the SH.

[55] For open ocean areas, we find a good agreement on the NH during NH winter, which supports the basic ideas of *Longuet-Higgins* [1950] and extends the findings of *Kedar et al.* [2008]. The high coherence thus provides a baseline for the interpretation of pattern yielding lower coherence.

[56] The resolution of modeled open ocean sources is globally homogeneous. In general, pelagic sources are concentrated in regions characterized by bathymetry-controlled, significant amplifications, predicted by theory (Figures 1b, 4, and 10). Excitation estimates are potentially inaccurate in regions of strong bathymetric variability, which violates the planar bottom assumption [*Longuet-Higgins*, 1950]. In particular, variations on scales smaller than the seismic wavelength reduce the effective area associated with an inferred resonance depth. The magnitude of the bias is expected to depend on wave

frequency, water depth, the properties of the seafloor relief, and the averaging techniques applied during bathymetry surveying and processing. Two broad regions, however, show consistently strong excitation over moderately amplifying ocean depths (west Pacific, Figure 5b; Tasman Sea, Figures 5b and 10). Complementary analyses of seismological records from the SH is needed to close existing observational gaps. Arrays in southern Africa and South America and Australia or New Zealand are expected to provide essential information to target remaining uncertainties of SH microseism excitation.

[57] The modeled systematic below average signal results from a lack of parametrization for coastal reflections, and good evidence exists that these do occur [*Elgar et al.*, 1994; *Graham et al.*, 2010; *Ardhuin et al.*, 2011]. For areas in which reflection coefficients would not produce an appreciable signal, alternative mechanisms might dominate microseism excitation. These include wind-driven, nonopposing wavefields [*Zhang et al.*, 2010], or mechanisms related to near-coastal surface current dynamics [*Kim et al.*, 2010]. For the case study of the North American east coast, we find that increased coastal energy follows the seasonal pattern, similar to open ocean excitation. Coastal amplitude estimates exceed offshore estimates only during periods of overall low activity, which emphasizes the dominance of the pelagic excitation mechanisms in the North Atlantic.

[58] An increased knowledge about the evolution of global spatiotemporal microseism excitation is expected to support noise-based imaging and monitoring in the corresponding frequency range. Time windows for the data analysis can be selected with respect to the target application, to improve the signal-to-noise ratio of the targeted correlation functions. Routinely provided catalogs of high-resolution hindcast WAM predictions supported by seismological observations are considered a valuable resource to guide choices of data selection.

[59] Such efforts can benefit from the consideration of a third independent observation on microseism-generating sea states, from estimates of microbarom source locations. Microbaroms constitute the atmospheric equivalence of microseisms. They are generated by the same mechanism, i.e., by oppositely traveling ocean gravity waves producing a standing pressure oscillation in the overlying gaseous column [*Posmentier*, 1967; *Arendt and Fritts*, 2000; *Waxler and Gilbert*, 2006]. The combined analysis of infrasound and seismological observations, together with WAM-predicted sea states patterns can further increase the robustness and reliability of microseism excitation estimates.

Acknowledgments

[60] We thank P. Roux for discussions on beamformer resolution. The manuscript benefited from the comments of the Editor, Thorsten Becker, and two anonymous reviewers. This work was supported by the European Research Council (advanced grant Whisper L27507). Most figures were constructed using Generic Mapping Tools (GMT) [*Wessel and Smith*, 1991].

References

Ardhuin, F., E. Stutzmann, M. Schimmel, and A. Mangeney (2011), Ocean wave sources of seismic noise, *J. Geophys. Res.*, *116*, C09004, doi:10.1029/2011JC006952.

Arendt, S., and D. C. Fritts (2000), Acoustic radiation by ocean surface waves, *J. Fluid. Mech.*, *415*, 1–21.

Aster, R. C., D. E. McNamara, and P. D. Bromirski (2010), Global trends in extremal microseism intensity, *Geophys. Res. Lett.*, *37*, L14303, doi:10.1029/2010GL043472.

Berger, J., P. Davis, and G. Ekström (2004), Ambient Earth noise: A survey of the Global Seismographic Network, *J. Geophys. Res.*, *109*, B11307, doi:10.1029/2004JB003408.

Brenguier, F., N. M. Shapiro, M. Campillo, V. Ferrazzini, Z. Duputel, O. Coutant, and A. Nercessian (2008), Towards forecasting volcanic eruptions using seismic noise, *Nat. Geosci.*, *1*, 126–130, doi:10.1038/ngeo104.

Bromirski, P. D., and F. K. Duennebier (2002), The near-coastal microseism spectrum: Spatial and temporal wave climate relationships, *J. Geophys. Res.*, *107*(B8), 2166, doi:10.1029/2001JB000265.

Bromirski, P. D., R. E. Flick, and N. Graham (1999), Ocean wave height determined from inland seismometer data: Implications for investigating wave climate changes in the NE Pacific, *J. Geophys. Res.*, *104*(C9), 20,753–20,766, doi:10.1029/1999JC900156.

Campillo, M. (2006), Phase and correlation of 'random' seismic fields and the reconstruction of the Green function, *Pure Appl. Geophys.*, *163*, 475–502, doi:10.1007/s00024-005-0032-8.

Cessaro, R. K. (1994), Sources of primary and secondary microseisms, *Bull. Seismol. Soc. Am.*, *84*, 142–148.

Courtland, R. (2008), Harnessing the hum, *Nature*, *453*, 146–148, doi:10.1038/453146a.

Elgar, S., T. H. C. Herbers, and R. T. Guza (1994), Reflection of ocean surface gravity waves from a natural beach, *J. Phys. Oceanogr.*, *24*, 1503–1511.

Froment, B., M. Campillo, P. Roux, P. Gouédard, A. Verdel, and R. L. Weaver (2010), Estimation of the effect of nonisotropically distributed energy on the apparent arrival time in correlations, *Geophysics*, *75*(5), SA85–SA93, doi10.1190/1.3483102.

Gerstoft, P., P. M. Shearer, N. Harmon, and J. Zhang (2008), Global P, PP, and PKP wave microseisms observed from distant storms, *Geophys. Res. Lett.*, *35*, L23306, doi:10.1029/2008GL036111.

Graham, N., R. W. Clayton, S. Kedar, F. Webb, and C. E. Jones (2010), Modeling microseism generation off southern

California with a numerical wave model: Coastal wave reflection and open ocean interactions, Abstract S13B-2017 presented at 2010 Fall Meeting, AGU, San Francisco, Calif., 13–17 Dec.

Gutenberg, B. (1924), Die seismischen Bodenunruhe, *Samml. Geophysikalischer Schr.*, *3*, 1–69.

Hasselmann, K. (1963), A Statistical analysis of the generation of microseisms, *Rev. Geophys.*, *1*(2), 177–210.

Haubrich, R. A., and K. McCamy (1969), Microseisms: Coastal and pelagic sources, *Rev. Geophys.*, *7*(3), 539–571.

Kedar, S. (2011), Source distribution of ocean microseisms and implications for time-dependent noise tomography, *C. R. Geosci.*, *343*, 548–557, doi:10.1016/j.crte.2011.04.005.

Kedar, S., M. Longuet-Higgins, F. Webb, N. Graham, R. Clayton, and C. Jones (2008), The origin of deep ocean microseisms in the North Atlantic Ocean, *Proc. R. Soc. A*, *464*, 777–793, doi:10.1098/rspa.2007.0277.

Kim, S. Y., et al. (2010), Mapping the U.S. West Coast surface circulation: A multiyear analysis of high-frequency radar observations, *J. Geophys. Res.*, *116*, C03011, doi:10.1029/2010JC006669.

Koper, K. D., and B. de Foy (2008), Seasonal anisotropy in short-period seismic noise recorded in South Asia, *Bull. Seismol. Soc. Am.*, *98*(6), 3033–3045, doi:10.1785/0120080082.

Koper, K. D., B. de Foy, and H. Benz (2009), Composition and variation of noise recorded at the Yellowknife Seismic Array, 1991–2007, *J. Geophys. Res.*, *114*, B10310, doi:10.1029/2009JB006307.

Landès, M., F. Hubans, N. M. Shapiro, A. Paul, and M. Campillo (2010), Origin of deep ocean microseisms by using teleseismic body waves, *J. Geophys. Res.*, *115*, B05302, doi:10.1029/2009JB006918.

Landès, M., L. Ceranna, A. Le Pichon, and R. Matoza (2011), Localization of infrasonic sources generated by the swell, *Geophys. Res. Abstr.*, *13*, Abstract EGU2011-3445.

Le Pichon, A., J. Vergoz, E. Blanc, J. Guilbert, L. Ceranna, L. Evers, and N. Brachet (2009), Assessing the performance of the International Monitoring System's infrasound network: Geographical coverage and temporal variabilities, *J. Geophys. Res.*, *114*, D08112, doi:10.1029/2008JD010907.

Longuet-Higgins, M. S. (1950), A theory of the origin of microseisms, *Philos. Trans. R. Soc. London, Ser. A*, *243*, 1–35.

Longuet-Higgins, M. S. (1953), Can sea waves cause microseisms?, in *Symposium on Microseisms Held at Arden House, Harriman, N. Y., 4–6 September, 1952*, pp. 74–86, Natl. Acad. of Sci., Washington, D. C.

McNamara, D. E., and R. P. Buland (2004), Ambient noise levels in the continental United States, *Bull. Seismol. Soc. Am.*, *94*(4), 1517–1527.

Meier, U., N. M. Shapiro, and F. Brenguier (2010), Detecting seasonal variations in seismic velocities within Los Angeles basin from correlations of ambient seismic noise, *Geophys. J. Int.*, *181*, 985–996, doi:10.1111/j.1365-246X.2010.04550.x.

Meier, W., J. Stroeve, F. Fetterer, and K. Knowles (2005), Reductions in Arctic sea ice cover no longer limited to summer, *Eos Trans. AGU*, *86*(36), 326, doi:10.1029/2005EO360003.

Mesquita, M. S., D. E. Atkinson, and K. I. Hodges (2010), Characteristics and variability of storm tracks in the North Pacific, Bering Sea, and Alaska, *J. Clim.*, *23*, 294–311, doi:10.1175/2009CLI3019.1.

Posmentier, E. (1967), A theory of microbaroms, *Geophys. J. R. Astron. Soc.*, *58*, 35–41.

Roux, P., K. G. Sabra, P. Gerstoft, W. A. Kuperman, and M. C. Fehler (2005), P-waves from cross-correlation of seismic noise, *Geophys. Res. Lett.*, *32*, L19303, doi:10.1029/2005GL023803.

Sabra, K. G., P. Gerstoft, P. Roux, W. A. Kuperman, and M. C. Fehler (2005), Surface wave tomography from microseisms in southern California, *Geophys. Res. Lett.*, *32*, L14311, doi:10.1029/2005GL023155.

Schimmel, M., E. Stutzmann, F. Ardhuin, and J. Gallart (2011), Polarized Earth's ambient microseismic noise, *Geochem. Geophys. Geosyst.*, *12*, Q07014, doi:10.1029/2011GC003661.

Schulte-Pelkum, V., P. S. Earle, and F. L. Vernon (2004), Strong directivity of ocean-generated seismic noise, *Geochem. Geophys. Geosyst.*, *5*, Q03004, doi:10.1029/2003GC000520.

Shapiro, N. M., and M. Campillo (2004), Emergence of broadband Rayleigh waves from correlations of the seismic ambient noise, *Geophys. Res. Lett.*, *31*, L07614, doi:10.1029/2004GL019491.

Shapiro, N. M., M. Campillo, L. Stehly, and M. H. Ritzwoller (2005), High-resolution surface-wave tomography from ambient seismic noise, *Science*, *307*, 1615–1618, doi:10.1126/science.1108339.

Smith, W. H. F., and D. T. Sandwell (1997), Global sea floor topography from satellite altimetry and ship depth soundings, *Science*, *277*, 1956–1962, doi:10.1126/science.277.5334.1956.

Stehly, L., M. Campillo, and N. M. Shapiro (2006), A study for the seismic noise from its long-range correlation properties, *J. Geophys. Res.*, *111*, B10306, doi:10.1029/2005JB004237.

Stutzmann, E., M. Schimmel, G. Patau, and A. Maggi (2009), Global climate imprint on seismic noise, *Geochem. Geophys. Geosyst.*, *10*, Q11004, doi:10.1029/2009GC002619.

Tanimoto, T. (2010), Equivalent forces for colliding ocean waves, *Geophys. J. Int.*, *181*, 468–478, doi:10.1111/j.1365-246X.2010.04505.x.

Tanimoto, T., S. Ishimaru, and C. Alvizuri (2006), Seasonality of particle motion of microseisms, *Geophys. J. Int.*, *166*, 253–266, doi:10.1111/j.1365-246X.2006.02931.x.

Tolman, H. L. (1999), User manual and system documentation of WAVEWATCH-III, version 1.18, *Tech. Note 166*, NOAA, Natl. Weather Serv., Natl. Cent. for Environ. Predict., Ocean Model. Branch, Boulder, Colo.

Tolman, H. L. (2005), Manual and user system documentation of WAVEWATCH-III, version 2.22, technical note, U.S. Dep. of Commer., Natl. Weather Serv., Natl. Cent. for Environ. Pred., Camp Springs, Md.

Waxler, R., and K. E. Gilbert (2006), The radiation of atmospheric microbaroms by ocean waves, *J. Acoust. Soc. Am.*, *119*(5), 2651–2664, doi:10.1121/1.2191607.

Webb, S. C. (2007), The Earth's "hum" is driven by ocean waves over the continental shelves, *Nature*, *445*, 754–756, doi:10.1038/nature05536.

Wegler, U., and C. Sens-Schönfelder (2007), Fault zone monitoring with passive image interferometry, *Geophys. J. Int.*, *168*, 1029–1033, doi:10.1111/j.1365-246X.2006.03284.

Wessel, P., and W. H. F. Smith (1991), Free software helps map and display data, *Eos Trans. AGU*, *72*(41), 441, doi:10.1029/90EO00319.

Wiechert, E. (1904), Verhandlungen der vom 24.-28. juli 1903 zu Strassburg abgehaltenen zweiten internationalen seismologischen Konferenz, in *Gerlands Beitrag Geophysik,*

Ergänzungsband II, edited by E. Rudolph, pp. 313–318, W. Engelmann, Leipzig, Germany.

Yang, Y., M. H. Ritzwoller, F.-C. Lin, M. P. Moschetti, and N. M. Shapiro (2008), Structure of the crust and uppermost mantle beneath the western united states revealed by ambient noise and earthquake tomography, *J. Geophys. Res.*, *113*, B12310, doi:10.1029/2008JB005833.

Yao, H., R. D. van der Hilst, and M. V. de Hoop (2006), Seismic-wave array tomography in SE Tibet from ambient seismic noise and two-station analysis - I. Phase velocity maps, *Geophys. J. Int.*, *166*, 732–744, doi:10.1111/j.1365-246X.2006.03028.x.

Zhang, J., P. Gerstoft, and P. M. Shearer (2009), High-frequency P-wave seismic noise driven by ocean winds, *Geophys. Res. Lett.*, *36*, L09302, doi:10.1029/2009GL037761.

Zhang, J., P. Gerstoft, and P. D. Bromirski (2010), Pelagic and coastal sources of *P*-wave microseisms: Generation under tropical cyclones, *Geophys. Res. Lett.*, *37*, L15301, doi:10.1029/2010GL044288.